Smart reinforcement steel bars with low-cost MEMS sensors for the structural health monitoring of RC structures

Smart reinforcement steel bars with low-cost MEMS sensors for the structural health monitoring of RC structures

F. Tondolo [1], A. Cesetti [1], E. Matta [2], A. Quattrone [1], D. Sabia [1].
[1] *Dept. Structural, Geotechnical and Building Eng., Politecnico di Torino – Italy, Email:* francesco.tondolo@polito.it
[2] *Dept. Architecture and Design, Politecnico di Torino – Italy*

Abstract

Structural health monitoring (SHM) of civil structures and infrastructures is increasingly drawing the attention of stakeholders and of the research community because of the emerging need in the optimal maintenance and management of the existing assets. The monitoring of reinforced concrete (RC) structures through measuring local strains is a valuable procedure but only a limited number of alternative technologies are currently available, mainly including electric strain gages and fibre optic sensors. The difficulty of their installation, the high cost of their sensing and/or interrogating equipment and their uncertain long-term reliability push for alternative low-cost and distributed systems, easier to install and use. This paper presents a new concept of an instrumented reinforcement steel bar, achieving strain-sensing capabilities through the incorporation of an ordinary low-cost embedded Micro Electro-Mechanical Systems (MEMS) sensor. According to this concept, a sealed cavity is made in the bar, filled with a fluid and hosting the MEMS sensor; the temperature and pressure readings collected by the MEMS sensor are used to evaluate the cavity volume variations and are thus correlated with the bar axial deformation. The proposed smart system shows significant advantages over current strain-measurement devices, proving cheap, durable, easy to install, robust to mechanical shocks and chemical aggression. The theoretical framework of the new concept and the results of a preliminary mechanical test campaign are here presented and discussed.

1. Introduction

Current advancements in the sensor research field are increasingly leading towards the acceptance and implementation of the "smart city" concept: an ultimate "nerves system" intended to monitor the various physical, chemical and biological aspects of manmade surroundings, which is expected to play in the near future a vital role in addressing the economic benefits and ethical needs for safe and sustainable structures and infrastructures around the world [1].

One crucial role in this concept will be played by the employment of appropriate structural health monitoring (SHM) strategies which, combining various sensing technologies with data acquisition and processing capabilities, will provide for a continuous condition assessment of civil engineering assets, increasing their quality and safety levels and reducing

their maintenance costs [2]. Long-term monitoring of degradation phenomena in aging structures will allow for the optimization of preventive maintenance policies and for the early detection of dangerous responses or incipient damages, thus reducing repair and down-time costs. On the other hand, the observation of the structural response after extreme events, such as earthquakes, hurricanes or fires, will allow for a rapid and objective assessment of the structural integrity.

Despite this great potential, SHM is still not applied at a large scale and in a systematic manner to civil structures and infrastructures. This is mostly due to the complexity and cost of monitoring large-scale constructions, which entails installing and interrogating large numbers of sensors as well as managing and interpreting huge amounts of data. In this context, the advancement in sensor technologies, the spread of smart materials and structures and the development of wireless communication platforms are the key opportunities for SHM growth, anticipating a future where every structure will be permanently, pervasively and (nearly-) automatically monitored since its construction [3].

Currently, various sensor types exist for SHM purposes, including electric strain sensors, piezoelectric sensors, GNSS-based sensors, accelerometers, inclinometers, acoustic emissions, wave propagation devices and various fibre optic sensors (FOS) of either distributed or local type, the latter including the well-known fibre Bragg grating (FBG) sensors [4-7]. Each of them has a preferable application field and presents genuine challenges when deployed in the real world. Recently, a growing use of low-cost MEMS sensors is observed which were initially developed for the consumer markets and are subsequently employed for SHM purposes, including accelerometers, inclinometers, temperature and humidity sensors [8].

Focusing on the SHM of reinforced concrete (RC) structures, and with the purpose of improving the cost-effectiveness of existing sensing technologies, this paper presents a new concept of smart reinforcing bar, called smart steel system (S3), achieving strain-sensing capabilities by incorporating a low-cost MEMS pressure and temperature sensor within a hermetic cavity drilled into the bar. By applying the well-known laws of thermodynamics, pressure and temperature measures are converted into cavity volume variations, eventually making the bar sensitive to longitudinal strains. S3 new sensing paradigm shows promising advantages over current sensing technologies. Its specific features and the results of a preliminary test campaign are presented in the following sections.

2 Current devices for strain measurement in RC structures

Strain monitoring of RC structures can be performed by focusing on either the concrete matrix or the steel bar. While steel is a homogeneous material, the concrete matrix presents non-uniform mechanical properties, which in fact require that the minimum size of concrete samples needed in macro-mechanical characterization tests is in the order of tens of

centimetres, i.e sufficiently larger than the maximum size of its constituent aggregates. When the scale of analysis is reduced, the micro-mechanical properties of concrete components, the influence of micro-cracking and rheological phenomena at smaller scales become very difficult to be managed. To account for these effects, any concrete-based measuring approach should employ either macro-sensors or small sensors mounted on macro skeletons, providing the average strain along the length of respectively the macro-sensor or the skeleton. In both cases, a perfect sensor-to-concrete adhesion is needed. On the contrary, the homogeneity of steel makes local strain measures insensitive to spatial variations of material properties and therefore representative of the average behaviour of the steel-concrete compound at the sensor location. This makes a local strain transducer placed on steel bars rather than immersed in the concrete matrix being generally preferred, because regarded as more accurate and reliable. In existing applications, such a local strain transducer can be either an electric strain gage glued on the longitudinal lug of the bar or a FOS, glued on the bar surface or incorporated in a longitudinal groove machined along the bar [9]. In both cases, compensation of temperature effects is needed. Critical stages for these applications are the sensor installation and the concrete pouring. Both strain gages and FOS can be damaged at these stages, or even during in-service operation as a consequence of cracks formation or steel-to-concrete slip. Furthermore, gluing of the sensor to the bar can be compromised by chemical aggression, mechanical action or ageing. In the case of FOS, the protective encapsulation, which is required to prevent standard glass fibres from the contact with the alkaline environment of the concrete mixture, results in a difference between the actual strain of the concrete matrix and the strain sensed by the fibre [10]. Moreover, the installation of distributed FOS requires specialized personnel, and the gluing process can be particularly time-demanding [11]. FOS systems require a particular care on cleanliness of terminal connectors to avoid interferences due to dust. Furthermore, in FOS applications the cost of the interrogating unit is often so high that only one unit can be afforded to be used on a structure, or even on different structures, thus resulting in significant constraints on the FOS usage.

3 The new sensing paradigm

When monitoring the strain of a bar in an RC structure, the strain transducer is usually placed along the bar surface. In a building site, this typically exposes the transducer to a harsh environment before, during and after its installation. Placing the transducer on the bar surface has also the inconvenient of locally altering the interaction mechanism at the interface between concrete and steel. Embedding sensors within the bar can potentially solve both problems. This approach was followed by Mains in his experimental work on bond tests [12]. In order not to perturb the concrete-steel

adhesion, Mains cut longitudinally the bars and placed strain gages in a longitudinal groove before welding again the two parts. This procedure proves particularly effective and has been recently used again in Lagier et al. [13].

Embedding the transducer in the bar is also at the core of the new S3 system proposed in this paper, although S3 develops the concept in a different way. In fact, the basic idea of S3 is to use low-cost existing micro-sensing devices, commonly used for other purposes, to estimate the strain in RC structural elements, by exploiting the mechanical laws of deformable continuum systems. According to this idea, an appropriate MEMS sensor is embedded in a small cavity drilled in its core and sealed by means of a proper closure system. Consequently, except for the required connections for data and power, the core of the system is within a "steel safe" and virtually aseptic environment. The sensor simultaneously measures both the pressure and the temperature of the fluid contained in the cavity. Any elongation or shortening of the bar will result in a variation of the cavity volume, according to the structural mechanics laws, which on its turn will determine pressure and/or temperature variations in the cavity. By measuring the latter variations through the sensor, the volume variation can be estimated by applying the appropriate thermodynamic state equations to the fluid contained in the cavity, and the axial elongation can be consequently deduced through a calibration process.

In greater detail, as long as the fluid is air, the thermodynamic state equation can be approximated by the ideal gas law as follows:

$$pV = nRT \tag{1}$$

where $p = p(t)$ is the absolute pressure in the cavity, $V = V(t)$ is the cavity volume, n is the number of moles of the fluid in the volume, R is the ideal gas constant, $T = T(t)$ is the absolute temperature within the cavity, and t is time.

Denoting as ΔV, Δp and ΔT the variations of the three state variables with respect to their initial values V_0, p_0 and T_0 at $t = 0$, and taking into account that n and R are constant parameters, any volume deformation $\Delta V/V_0$ can be generally computed, at any time t, from the monitored time histories of p and T, as follows:

$$\frac{\Delta V}{V_0} = \left(1 + \frac{\Delta T}{T_0}\right) \Big/ \left(1 + \frac{\Delta p}{p_0}\right) - 1 \tag{2}$$

In general, the volume deformation $\Delta V/V_0$ of the cavity reflects any local axial deformation of the bar, no matter if due to mechanical, thermal, rheological or other reasons. In this paper, coherently with the presented experimental tests, $\Delta V/V_0$ is assumed to be potentially caused by mechanical and/or thermal actions only. Also, for the sake of simplicity, the part of $\Delta V/V_0$ caused by mechanical actions is assumed to be expressible as a function of the bar axial force variations, which is always the case for a bar subjected to axial loads except when it exhibits perfectly plastic

deformations right before rupture. Denoting by ΔF any variation of the bar axial load F (with respect to its initial value F_0) and by ΔT_b any variation of the bar temperature T_b (with respect to its initial value T_{b0}), and assuming for simplicity a linear superposition of the mechanical and thermal effects, this concept can be formalized as follows:

$$\frac{\Delta V}{V_0} = \left(\frac{\Delta V}{V_0}\right)_{\Delta F} + \left(\frac{\Delta V}{V_0}\right)_{\Delta T_b} \tag{3}$$

where $(\Delta V/V_0)_{\Delta F}$ is the volume deformation due to the bar axial force variations ΔF and $\left(\Delta V/V_0\right)_{\Delta T_b}$ is the volume deformation due to the bar temperature variations ΔT_b. It is worth noticing that ΔT and ΔT_b may generally not coincide, since the former is the temperature of the fluid in the cavity, while the latter is the average bar temperature, responsible for the whole bar thermal deformations.

Complemented by Eq. (2), Eq. (3) plays a fundamental role both at the stage of system calibration, which includes a preliminary thermal calibration and a subsequent mechanical calibration, and at the stage of sensor operation, i.e. during monitoring.

The preliminary thermal calibration tests have the scope of applying controlled temperature variations ΔT_b to the mechanically unloaded bar ($\Delta F = 0$). In these conditions, in facts, the first term of the right-hand side of Eq. (3), i.e. $(\Delta V/V_0)_{\Delta F}$, is null, and Eq. (3) directly provides the experimental relation $f(\cdot)$ existing between ΔT_b and $\left(\Delta V/V_0\right)_{\Delta T_b}$ as follows:

$$\left(\frac{\Delta V}{V_0}\right)_{\Delta T_b} = \left.\frac{\Delta V}{V_0}\right|_{\Delta F=0} = f\left(\Delta T_b\right) \tag{4}$$

where $\Delta V/V_0|_{\Delta F=0}$ is the volume deformation computed according to Eq. (2) on the bases of the measured pressure and temperature variations Δp and ΔT. As long as temperature variations are slow during thermal tests, the bar temperature ΔT_b can be assumed equal to the cavity temperature ΔT, so that in this case no additional temperature transducers are required for calibration beyond the embedded one.

The subsequent mechanical calibration tests have the scope of applying controlled axial force variations ΔF to the bar and are usually conducted in uncontrolled temperature conditions. Because temperature variations cannot be avoided, Eq. (3) must be complemented by both Eq. (2) and Eq. (4) in order to provide the experimental relation $g(\cdot)$ existing between ΔF and $(\Delta V/V_0)_{\Delta F}$:

$$\left(\frac{\Delta V}{V_0}\right)_{\Delta F} = \frac{\Delta V}{V_0} - f(\Delta T_b) = g(\Delta F) \tag{5}$$

where $\Delta V/V_0$ is computed according to Eq. (2) based on measured Δp and ΔT values, and $f_1(\Delta T_b)$ is computed according to Eq. (4) based on measured ΔT_b values. Notice that, because temperature variations ΔT induced in the cavity by sudden axial force variations need to be transferred to the bar and eventually dissipated, ΔT_b and ΔT do not generally coincide in this case, and separate measurements would be in principle required (e.g. through adding a further temperature sensor which measures the bar temperature) if a continuous accurate tracking of the axial force time history was required.

As long as the bar responds in its linear elastic range and mechanical deformations keep small, a proportional relation is expected between the axial force and the volume deformation, which can be finally expressed by:

$$\left(\frac{\Delta V}{V_0}\right)_{\Delta F} = g(\Delta F) = \frac{1}{k}\Delta F \tag{6}$$

where k is the mechanical calibration coefficient transforming the measured volume variation (corrected by Eq. (5)) into the estimated axial load.

If mechanical deformations become large and the bar responds in its nonlinear range, the linear relation expressed in Eq. (6) is no longer applicable. In this case, the function $g(\Delta F)$ still can be identified through experiments, but becomes highly nonlinear and strongly dependent on the tested bar sample, thus lacking representativeness for calibration purposes. Alternatively, instead of looking for a direct correlation between $(\Delta V/V_0)_{\Delta F}$ and ΔF, a relation could be searched between $(\Delta V/V_0)_{\Delta F}$ and the bar elongation, the latter providing a complete and more stable representation of the bar mechanical conditions. This point will be better explained in the next sections when discussing the results of the experimental campaign.

Eqs. (4) to (6) express the desired thermal and mechanical calibration relations. Even more remarkably, Eqs. (5) and (6) also allows the estimation of the axial force ΔF during sensor operation, which is the main purpose of the monitoring action.

4 Description of the system

Measures of pressure and temperature in the bar cavity can be easily provided by commercial MEMS barometric sensors which usually integrate pressure and temperature transducers. Nowadays barometric MEMS are commonly employed in smartphones and smartwatches, IoT devices, wearable and fitness trackers and others, thanks to their small

dimensions (around 2x3x1 mm^3). These MEMS are easily available on the market at a cost of about 2 $ each. In the present version of S3, a commercial barometric ultra-compact piezoresistive pressure sensor is used. Its operating pressure and temperature ranges extend, respectively, from 260 hPa to 1260 hPa and from -30 °C to 105 °C. The smart steel system S3 is based on a Patent [14]. Although generally applicable to several other types of structural elements, S3 is here applied to the case of a ribbed steel bar in which a cavity is obtained in the shape of a transversal cylindrical drilled hole. The latter determines an internal volume, filled with air and hosting a hard PCB, on which the barometric sensor is mounted. An electrical feedthrough is provided at the entry of the cavity, connecting the hard PCB inside with a soft PCB outside, which on its turn communicates with the acquisition system, exchanging power and data. The cavity is hermetically sealed, and the soft PCB is lodged into a groove machined all along the longitudinal lug of the bar. Schematics of the system are reported in Figure 1. The cavity determines a reduction of the bar section which is a critical point for stress increase and concentration. The consequent reduction in resistance and/or ductility may not represent a significant drawback, as the exact reproduction of the original bar mechanical properties is deemed inessential at this stage of development.

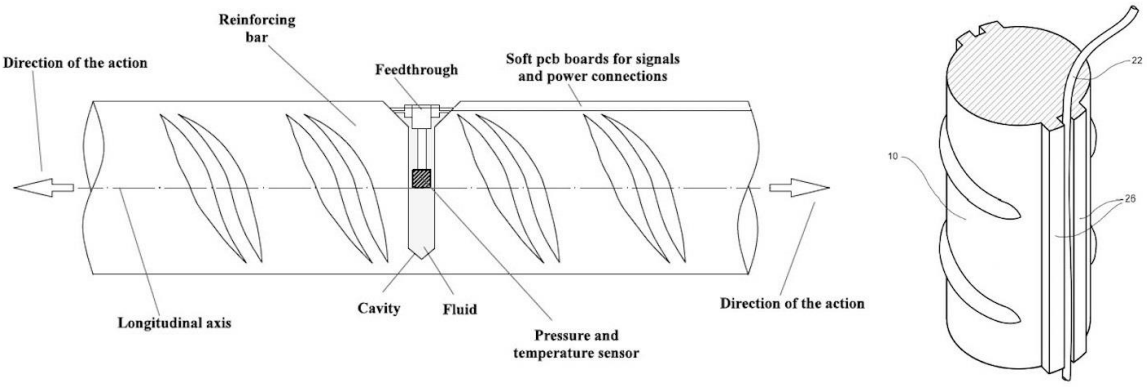

Fig. 1. Longitudinal view with section at the system location (left) and axonometric view of the soft PCB hosted in the bar lug (right). Picture from [14].

5. The Experimental Campaign

5.1 Description of the setup components

The experimental tests focus on a ribbed steel bar instrumented with the monitoring system described in the previous paragraphs. Figure 2 shows the system setup during tests. The bar has a 20 mm diameter and is equipped with three measuring units spaced 80 mm from each other, respectively called S_1, S_2 and S_3. Each unit is hosted within a cylindrical drilled hole, 4 mm in diameter and 18 mm in depth. A closer look at the ingress of one unit is provided in Figure 2a. A longitudinal groove, 2 mm deep and 2 mm wide, is machined into the bar and hosts the soft PCBs which connect the pins of the feedthrough to the converter boards, fixed at the lower grip as clearly visible at the bottom of

Figure 2b. The converter boards acquire the digital pressure and temperature data coming from the embedded sensors and transform them into analogue continuous voltage signals collected by the acquisition system.

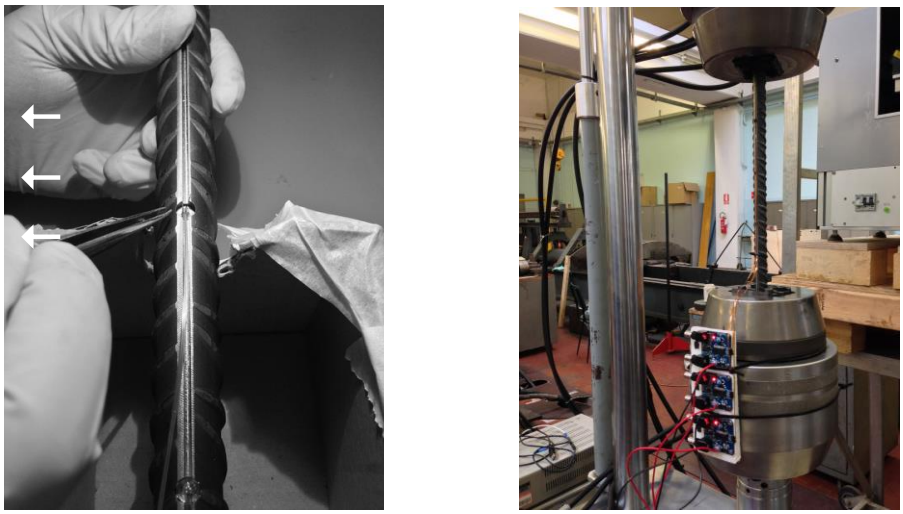

(a) (b)

Fig. 2. The experimental setup.

5.2 Thermal calibration tests

Thermal calibration tests are preliminarily conducted by subjecting the instrumented bar to temperature variations at zero axial load, in order to get, for each measuring unit, the experimental relation $f(\cdot)$ between ΔT_b and $\left(\Delta V/V_0\right)_{\Delta T_b}$, according to Eq. (4). The bar, placed in a temperature controlled chamber, is subjected to various cycles of slow temperature variations (1°C/10min), approximately spanning 27°C between 14.5°C and 41.5°C. Figures 3a, 3b and 3c show a comparison between the experimental curves and their cubic interpolations, for the three measuring units. A negligible hysteresis with repeated thermal loading cycles can be appreciated. The relations are clearly nonlinear and monotonically decreasing. The decreasing trend is a counterintuitive result still deserving an explanation, which probably resides in the complexity of the thermo-mechanical coupling of structural and non-structural components involved in the cavity, including in particular the bar, the sensor and the feedthrough. Anyway, the decreasing trend is confirmed by all the numerous tests so far performed on different measuring units and different bars, and its application according to Eq. (5) systematically provides a substantial correction of the environmental temperature trends in axial load tests. Figure 3d compares the $f(\cdot)$ relations identified for the three measuring units. They appear similar in trend but far from identical, suggesting that the thermal calibration must be conducted for every measuring unit, at least at the present stage of early-bird development of the system.

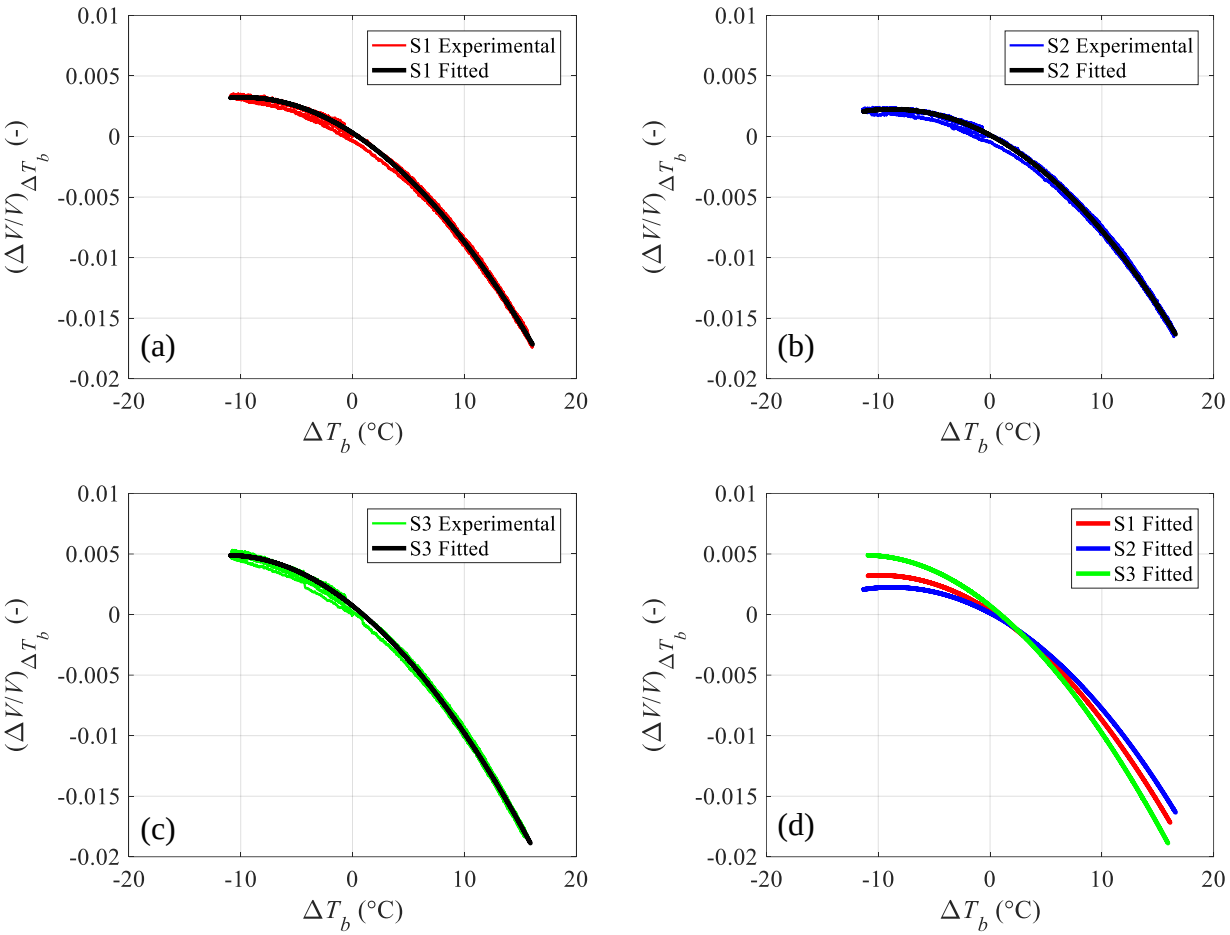

Fig. 3. Thermal compensation: determination of the $f(\cdot)$ relation between ΔT_b and $(\Delta V/V_0)_{\Delta T_b}$, through fitting the experimental data obtained in a temperature controlled environment, for the three sensors.

5.3 Axial load tests in the linear elastic range

The same instrumented bar previously examined is subjected to uniaxial tensile load tests, conducted within its linear elastic range in uncontrolled thermal conditions. The load is imparted through a universal testing machine having a maximum load capacity of 250 kN (partly visible in Figure 2b). Considering the dimensions of the holes hosting the sensors and the presence of the longitudinal groove, the bar transversal section centred on the hole is about 24% smaller than the nominal section. In order to avoid the insurgence of any plastic strain during the tests due to the effect of the holes, the maximum applied load is limited to 40 kN, assuming a stress intensity factor equal to 3.

The first test (axial load test #1) is used to establish the necessary mechanical calibration of the three measuring units. To this purpose, a complete loading and unloading cycle is performed through 8 steps of 5 kN each, corresponding to about 20 MPa of tensile stress on the bar net transversal section. The load variations are applied instantaneously and maintained for about 120 s. According to Eq. (6), this test provides the mechanical calibration coefficients k_1 = $3.0162 \cdot 10^4$ kN, k_2 = $2.0396 \cdot 10^4$ kN and k_3 = $2.4823 \cdot 10^4$ kN, respectively for the three measuring units. In Figure 4 the

time histories are reported for, respectively, the applied force (4a), the measured pressure (4b) and temperature (4c) normalized variations, the corrected volume variations (4d), the volume-to-force calibration functions for respectively S_1 (4e), S_2 (4f) and S_3 (4g), and the comparison between the applied and the estimated axial force (4h).

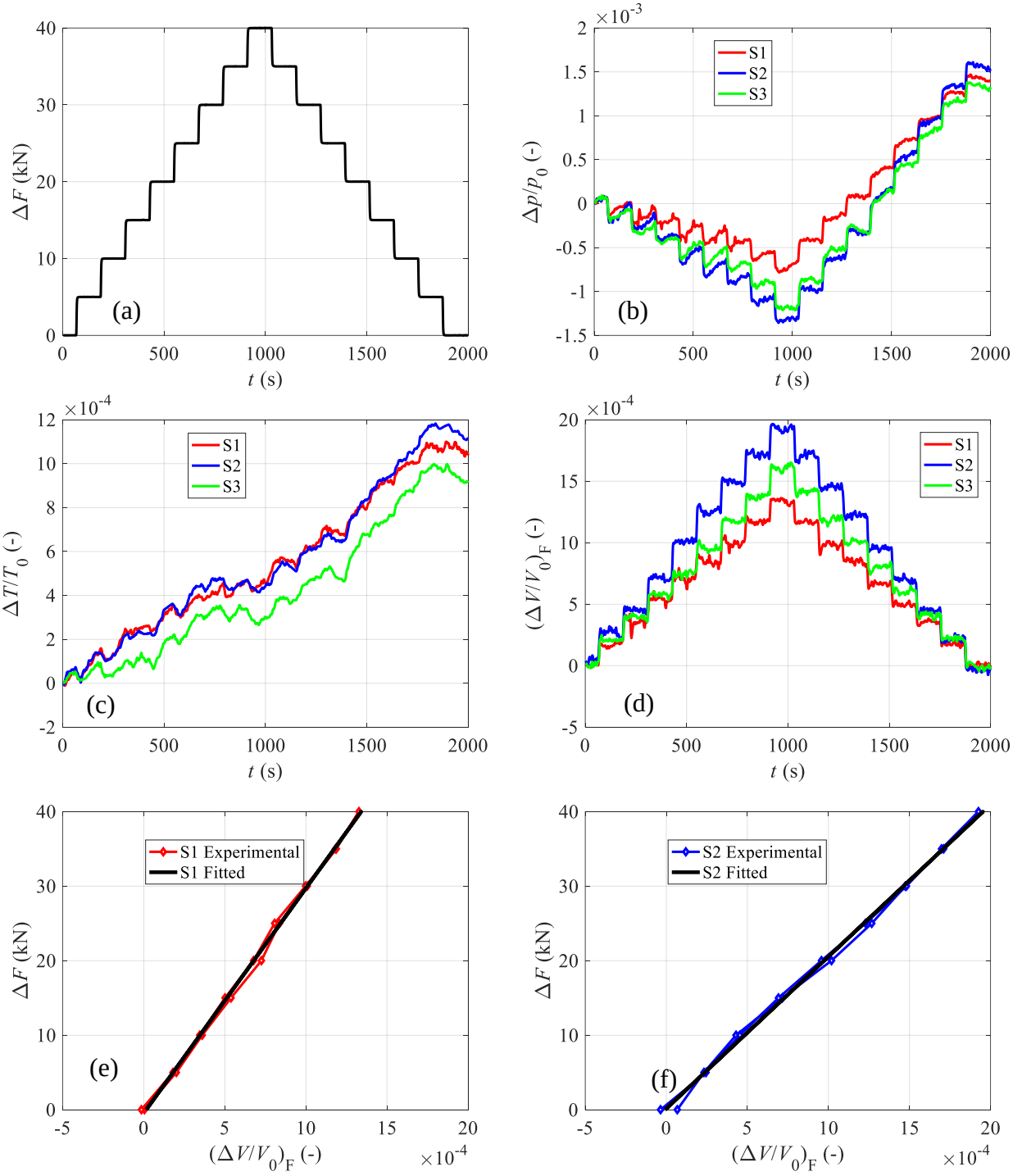

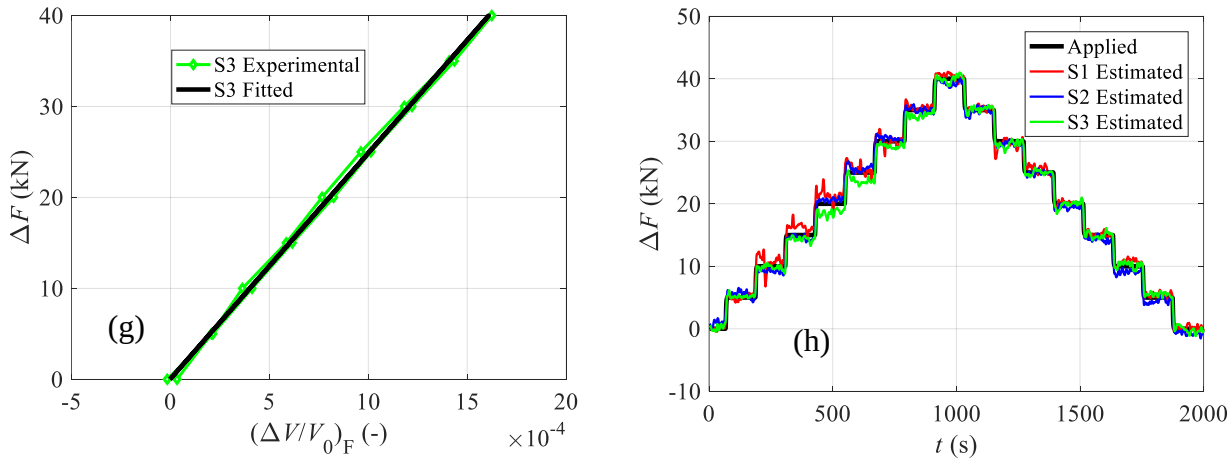

Fig. 4. Axial load test #1: (a) applied force; (b) measured pressure; (c) measured temperature; (d) reconstructed force-dependent volume variation; (e) volume-to-force calibration for sensor S_1; (f) volume-to-force calibration for sensor S_2; (g) volume-to-force calibration for sensor S_3; (h) applied vs estimated force.

Subsequently, seven load tests are conducted by subjecting the same instrumented bar to a series of alternative force time-histories, with the aim to verify the accuracy of the axial load estimation in different loading conditions. In particular, axial load test #2 (Figure 5) presents three consecutive one-step loading/unloading cycles of increasing amplitude (respectively 10, 20 and 40 kN); axial load test #3 (Figure 6) presents the same multi-step loading/unloading cycle already applied in axial load test #1, although reduced by half in amplitude and applied both in tension and in compression (with a maximum load of ±20 kN); axial load tests from #4 to #7 (Figures 7 to 10) present one or more sinusoidal loading/unloading cycles of variable amplitude and period, according to Table 1.

Table 1. Sinusoidal axial load tests #4 to #7

Test number	Number of cycles	Amplitude (kN)	Period (s)
4	1	20	1000
5	2	10	250
6	10	10	50
7	20	10	20

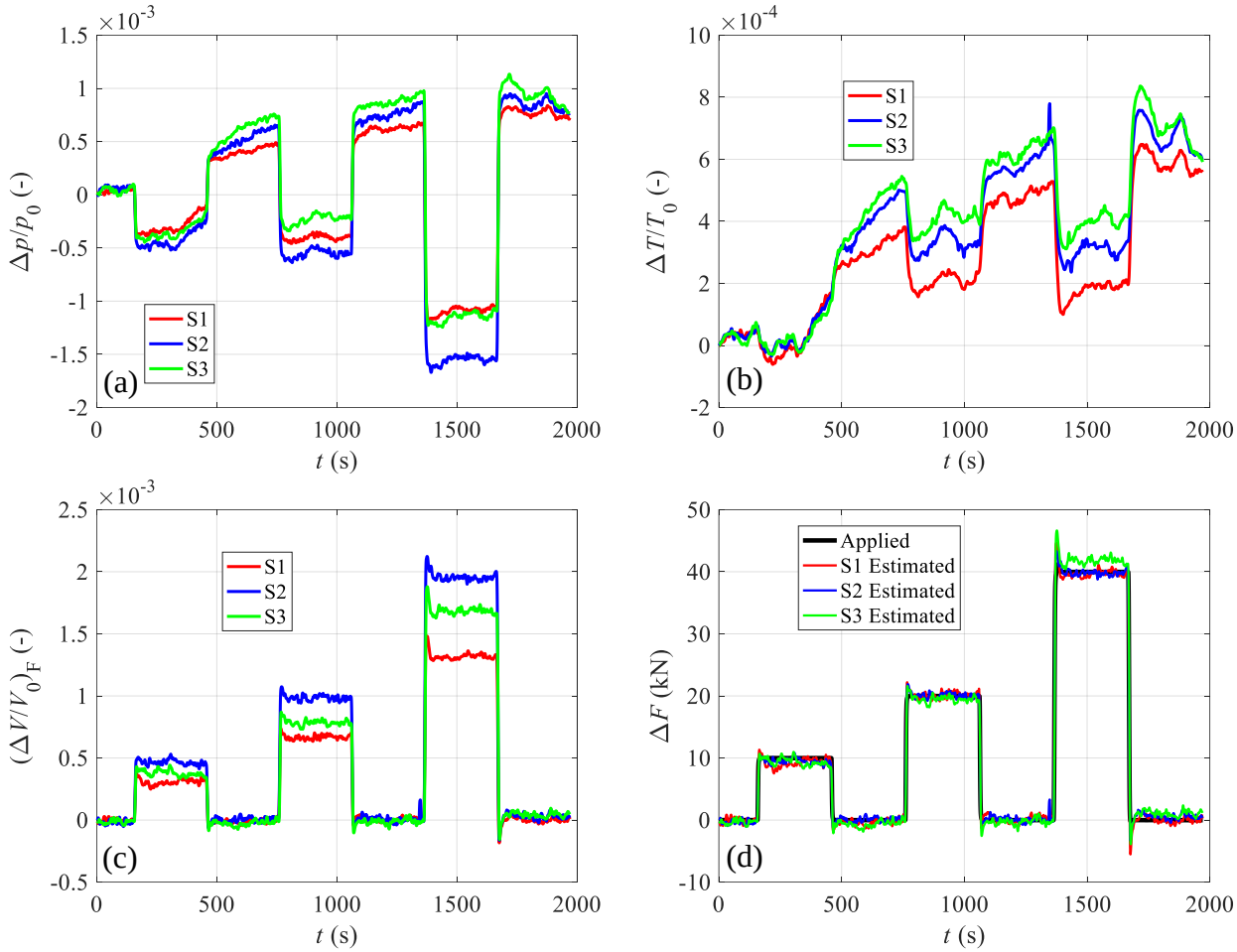

Fig. 5. Axial load test #2: (a) measured pressure; (b) measured temperature; (c) reconstructed force-dependent volume; (d) applied vs estimated force. Note: volume-to-force calibration as from test #1.

In all tests, a satisfactory estimation of the applied axial load is obtained, whether the latter is imparted in tension only or both in tension and in compression. Minor deviations appear only in the presence of rapid load variations, due either to sudden load steps (e.g. in axial load test #2, see Figure 5) or to cyclic loads conducted at relatively high frequency (e.g. in axial load test #7, see Figure 10). In these circumstances, the dynamic character of the load input does not allow for a sufficient stabilization of the cavity temperature measurements, implying an imperfect tracking of the imparted load. Even so, the estimated load time-history provides an average value of the sinusoidal amplitude which is quite similar to the actual one. Referring in particular to test #1, a substantial proportionality and a negligible hysteresis can be appreciated in the volume-to-force relations (Figures 4e, 4f and 4g).

To quantify the error between the applied and the estimated force time histories, Table 2 summarizes the measuring errors computed for each test, distinguished in zero errors and mean errors. Denoting by $e(t) = \Delta F_e(t) - \Delta F_a(t)$ the instantaneous absolute error at time t, i.e. the discrepancy at time t between the estimated force ΔF_e and the applied force ΔF_a, the zero error ZE is defined as the mean value of the average absolute errors computed respectively before

($\bar{e}_{ini}$) and after ($\bar{e}_{end}$) the loading/unloading cycle (i.e. at zero load conditions), normalized to the maximum applied load $\Delta F_{a,max}$. In formulas:

$$ZE = \frac{mean(\bar{e}_{ini}, \bar{e}_{end})}{\Delta F_{a,\max}} \tag{7}$$

On the other hand, denoting by $e_r(t) = e(t)/\Delta F_a(t) = \Delta F_e(t)/\Delta F_a(t) - 1$ the instantaneous relative error at time t, the mean error *ME* is defined as the average relative error computed under all significant applied forces, i.e. under forces larger than a given threshold force here chosen as $\Delta F_{a,thr}$ = 0.314 kN (in fact corresponding to 1 MPa of axial stress in the nominal bar section without the cavity). In formulas:

$$ME = \bar{e}_r \ , \quad \forall t \ | \Delta F_a(t) > \Delta F_{a,thr} \tag{8}$$

In all tests, and particularly in tests #1 and #4, a temperature drift ΔT_b is visible during testing, certainly attributable to environmental effects. A temperature variation ΔT is also measured inside the cavity during the test, as a result of the nearly-adiabatic thermodynamic process occurring inside the cavities during high-rate loading variations (prior to the initiation of the heat conduction process). Presently, not enough experimental information is available to discriminate between the effects of, respectively, ΔT_b and ΔT on the thermal calibration (Eq. 4), in the case when ΔT_b and ΔT do not coincide. For simplicity, Eq. (5) has been here applied by assuming $\Delta T_b = \Delta T$, but further in-depth investigations are necessary on this aspect, possibly requiring the installation of further temperature sensors within (or on the surface of) the bar. This is left for future work.

It is important to point out that the whole system, including sensor and acquisition system, is not currently optimized to handle high deformation rate or dynamic loads.

Table 2. Zero error *ZE* and mean error *ME* for the seven tests

Test	Zero error (ZE) (%)			Mean error (ME) (%)		
	S1	S2	S3	S1	S2	S3
#1	-0.09%	-1.03%	-0.37%	-2.99%	1.65%	0.41%
#2	0.13%	0.75%	1.49%	2.65%	1.30%	1.46%
#3	-0.71%	-3.20%	-2.88%	-4.34%	-2.98%	-3.81%
#4	-3.62%	-3.41%	0.43%	1.83%	5.63%	3.75%
#5	3.21%	1.42%	0.91%	7.49%	2.62%	-0.03%
#6	3.61%	-2.20%	-2.57%	-6.51%	-5.67%	-10.08%
#7	0.71%	2.61%	-0.74%	-8.45%	-5.73%	-9.44%

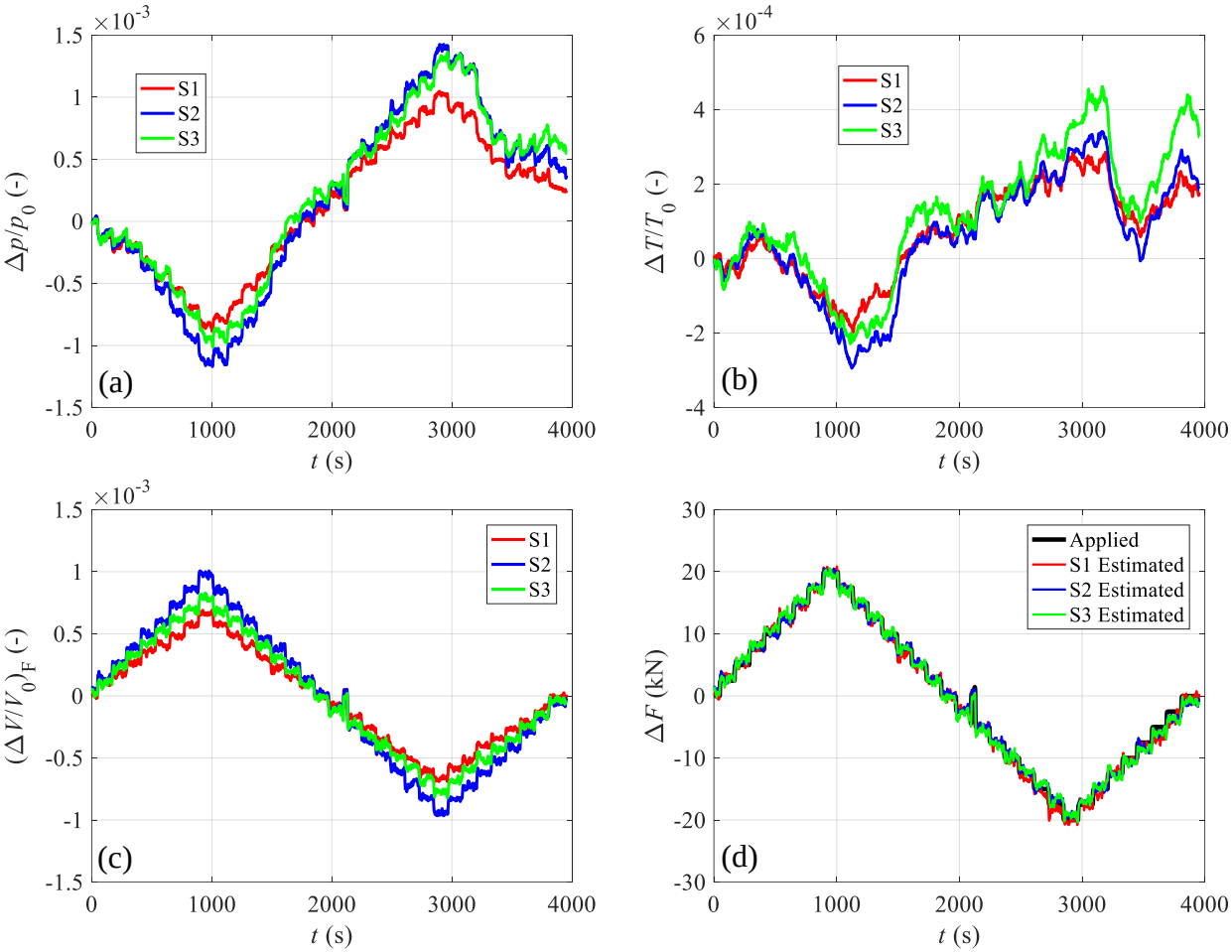

Fig. 6. Axial load test #3: (a) measured pressure; (b) measured temperature; (c) reconstructed force-dependent volume; (d) applied vs estimated force. Note: volume-to-force calibration as from test #1.

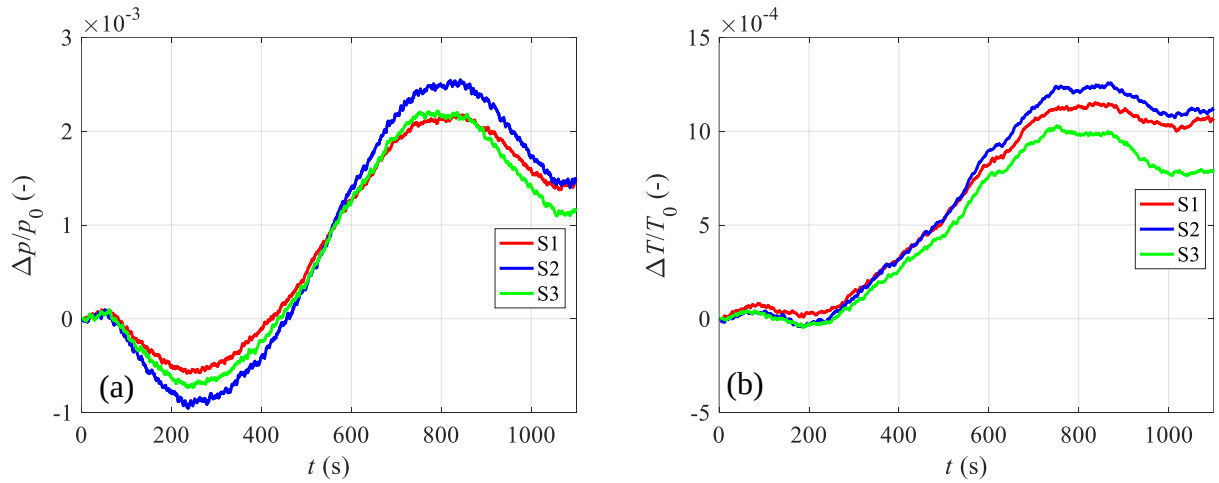

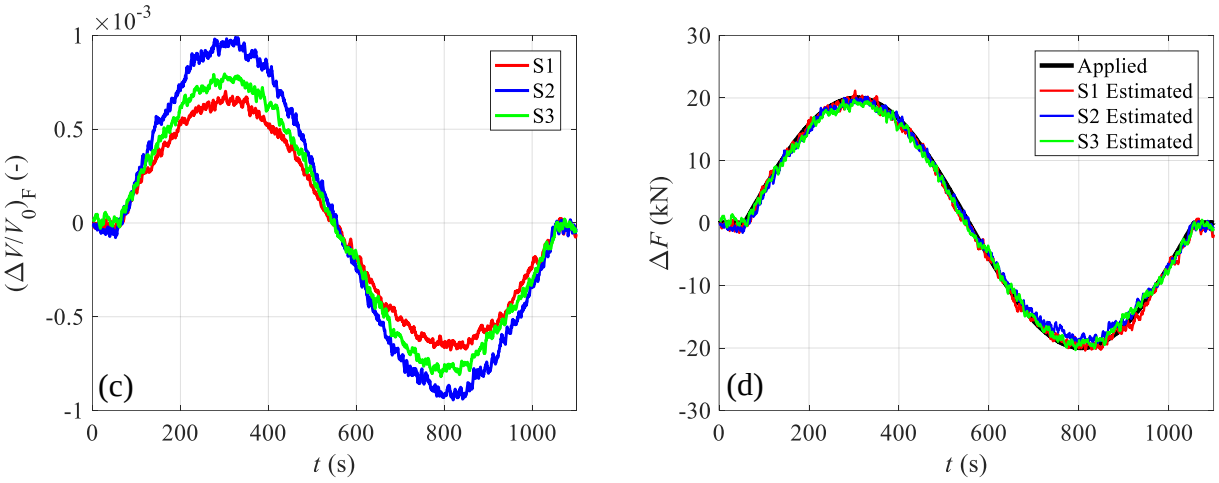

Fig. 7. Axial load test #4: (a) measured pressure; (b) measured temperature; (c) reconstructed force-dependent volume; (d) applied vs estimated force. Note: volume-to-force calibration as from test #1.

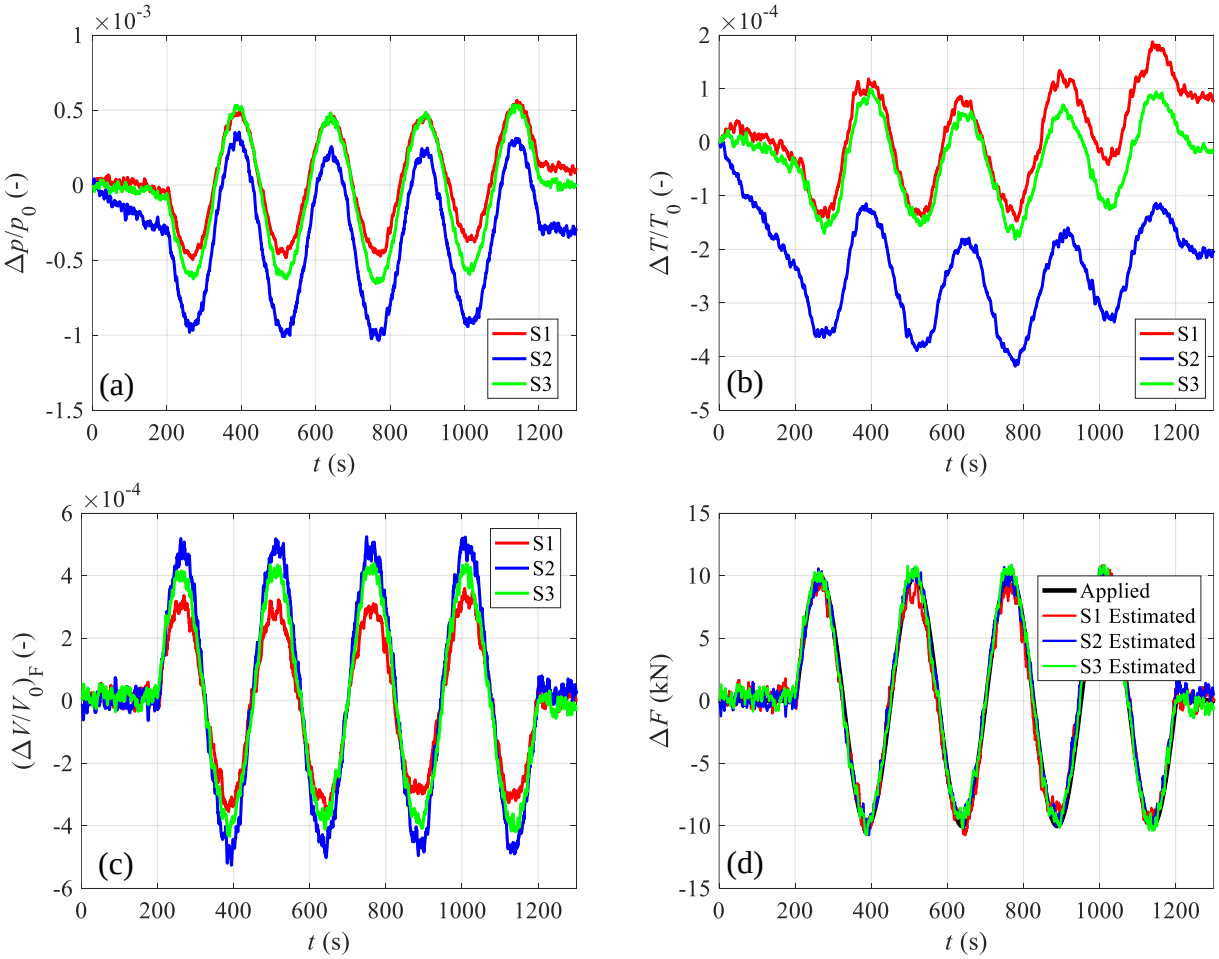

Fig. 8. Axial load test #5: (a) measured pressure; (b) measured temperature; (c) reconstructed force-dependent volume; (d) applied vs estimated force. Note: volume-to-force calibration as from test #1.

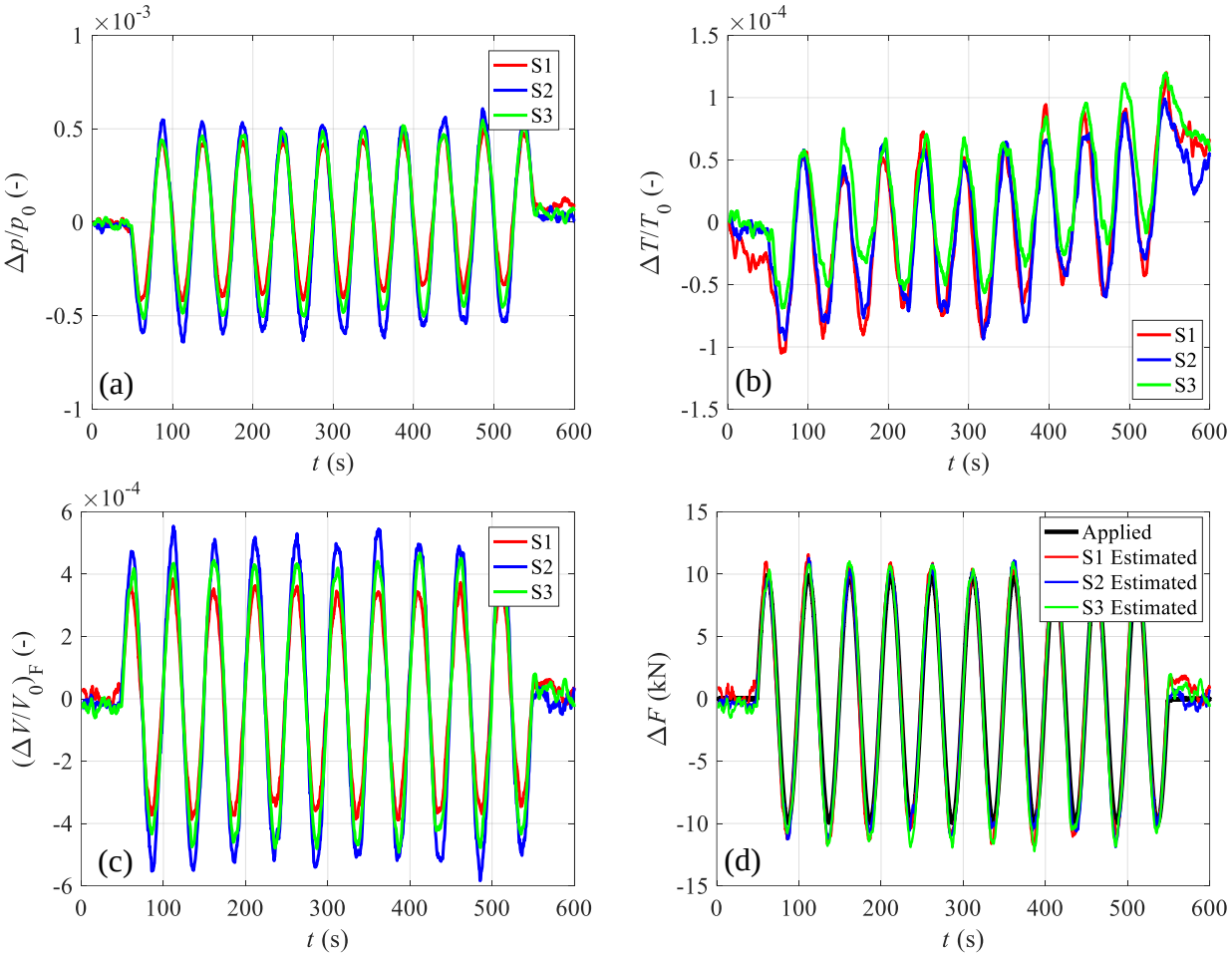

Fig. 9. Axial load test #6: (a) measured pressure; (b) measured temperature; (c) reconstructed force-dependent volume; (d) applied vs estimated force. Note: volume-to-force calibration as from test #1.

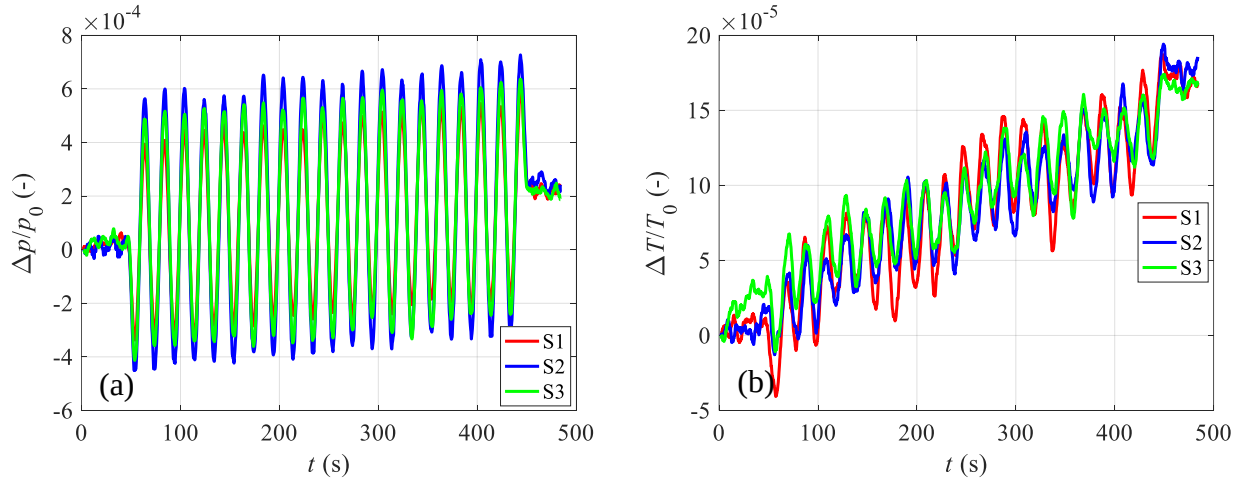

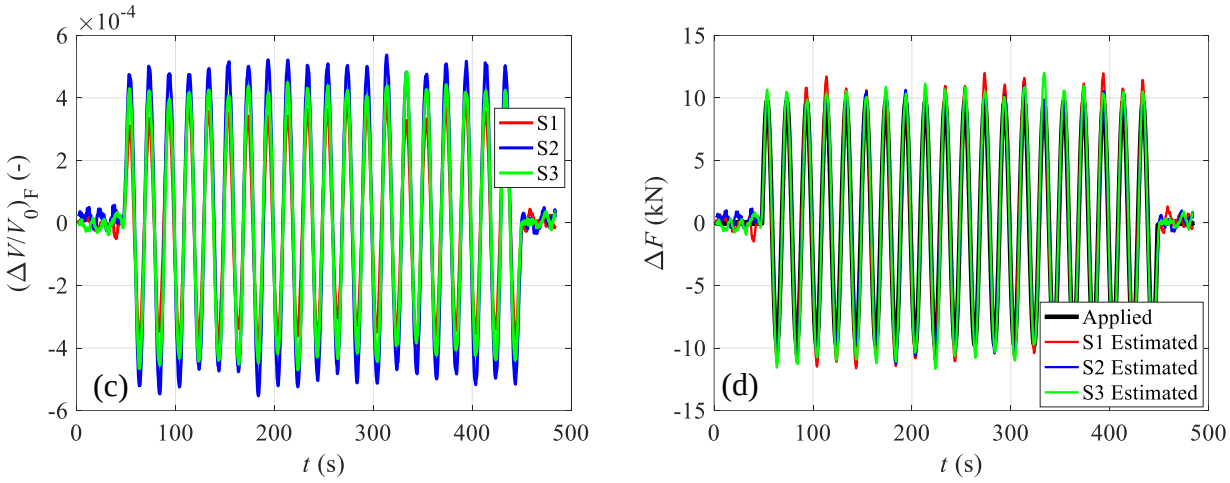

Fig. 10. Axial load test #7: (a) measured pressure; (b) measured temperature; (c) reconstructed force-dependent volume; (d) applied vs estimated force. Note: volume-to-force calibration as from test #1.

5.4 Axial tensile test until rupture

The same instrumented bar is finally subjected to a monotonic uniaxial tensile test until rupture in order to analyse its response after yielding.

To predict its mechanical response under such a test, and particularly the influence of the cavity on the yield strength, the ultimate strength and the ductility of the bar, preliminary rupture tensile tests are first conducted on non-instrumented bars hosting a single transversal through hole. This preliminary test also helped in defining the amplitude of the load steps during the axial tests of the instrumented bar. Figure 11 refers to a 20mm bar in which a cylindrical through hole has been drilled having a 4mm diameter. Figure 11a shows the deformed cavity just before rupture, clearly highlighting the concentration of plastic strains around the hole. Figure 11b shows the cavity area after rupture. The yield strength and the ultimate strength appear to be reduced by around 21% and 19%, respectively, with respect to a sound bar sample coming from the same lot. Considering the 24% reduction of the drilled section, this means that a slight increase in the yield and ultimate stresses is observed. The ductility appears, instead, to be more significantly reduced.

(a) (b)

Fig. 11. Preliminary tensile test until rupture of a non-instrumented bar with a single cylindrical through hole: (a) before rupture; (b) after rupture.

The instrumented bar is then tested until rupture (Figure 12). For comparison with the measurements provided by units S_1, S_2 and S_3, three high-accuracy strain transducers are also positioned across the cavities on the bar, measuring the axial elongation ΔL_i (i = 1 to 3) of the bar over a length of 25 mm around each unit (Figure 12a). Rupture occurs in correspondence to the upper of the three cavities (S_3 in Figure 12b).

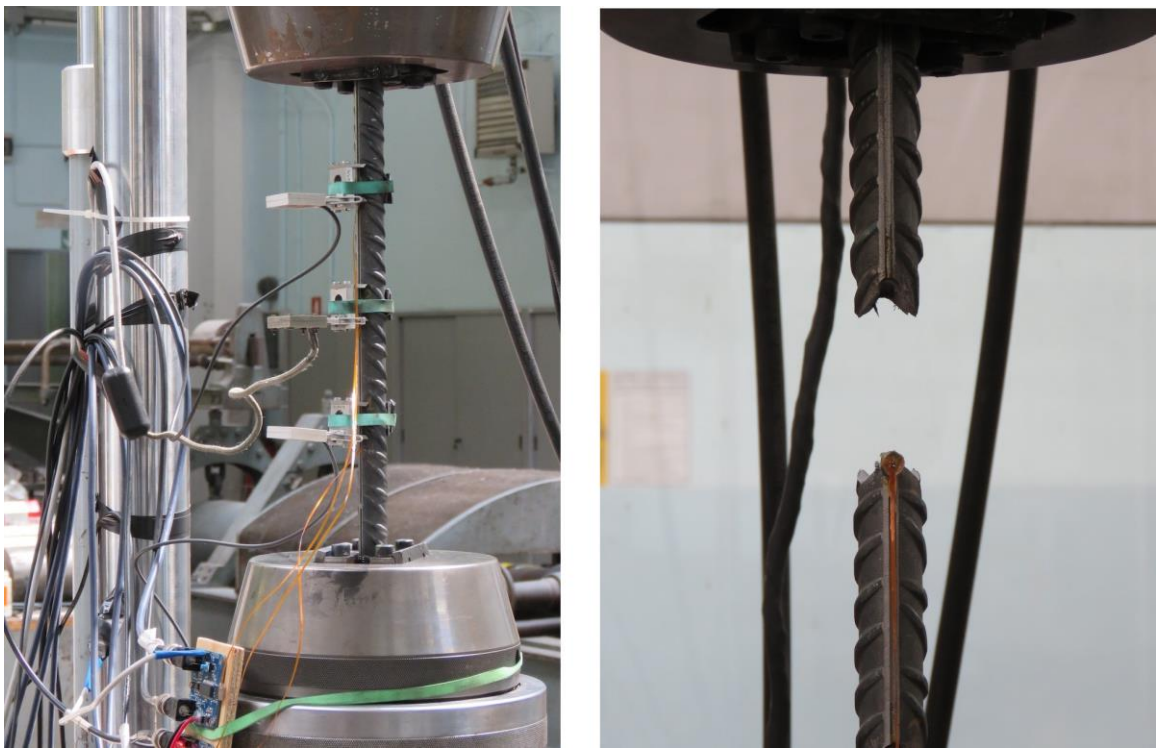

Fig. 12. Monotonic tensile test until rupture of the instrumented bar.

Results are reported in Figures 13 to 15. Figures 13a and 13b show the time histories of the applied axial load and the output of the three strain transducers, respectively. Figure 13c shows the corresponding force-displacement relations for the three strain transducers. The tensile test is conducted by assigning a displacement control time history to the bar through the test machine, with a displacement rate manually varied during the test depending on the current response of both the bar and the sensing equipment (Figure 13b). In particular, the displacement rate is kept lower at the beginning of the test, when the bar structural behaviour is linear elastic and its tangential stiffness is maximum, and increased later, when significant inelastic deformations occur and the tangential stiffness decreases. Moreover, the displacement is stopped twice, respectively around 1000 s and 2000 s, in order to verify the state of the sensors, and another time later, around 2800 s, in order to remove the strain transducers before the bar rupture might possibly damage them. The resulting irregular elongation control law (Figure 13b) explains some irregularities in the load time history, clearly apparent in Figure 13a, and smaller ones in the load-displacement curves, visible in Figure 13c. The latter three curves describe an almost identical nonlinear trend, catching the local inelastic response of the bar across each cavity. This response appears substantially linear for approximately $\Delta F < 50$ kN, and begins experiencing large plastic deformations starting at about $\Delta F = 125$ kN, representing the local yielding of the bar around the cavities. At the instant of removing the three strain transducers, the applied load (155 kN) is only slightly less than the ultimate load reached during the test (159 kN) but the elongations (equal to about 4% over the 25mm base of the strain transducers) are still much less than their ultimate values obtained at rupture.

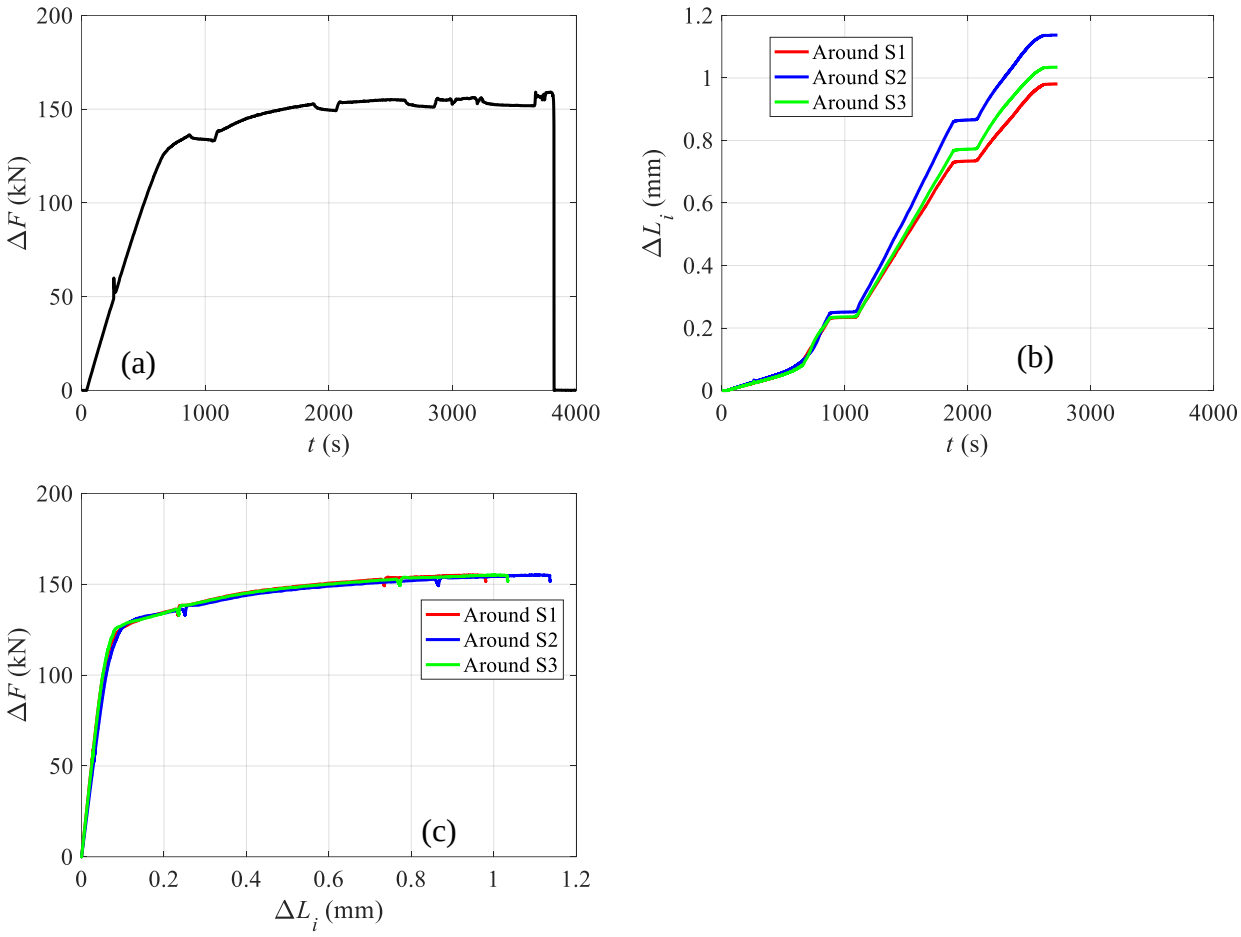

Fig. 13. Monotonic tensile test until rupture: (a) applied force; (b) elongations measured by the three strain transducers around each measuring unit; (c) force-displacement relations for the three strain transducers.

Figure 14 shows the results obtained from the three S_1, S_2 and S_3 measuring units. In complete analogy with Figures 5 to 10, Figure 14 reports the time histories of, respectively, the measured pressure and temperature variations (Figures 14a and 14b), the reconstructed force-dependent volume variations (Figure 14c) and the applied versus the estimated force variations (Figure 14d). With respect to the results obtained from the previously described linear elastic tests, however, two main differences are observed. The first, most evident difference is the failure of the sealing system occurring for S_1, S_2 and S_3 at approximately t = 850 s, 1500 s and 1850 s, respectively. Sealing failure corresponds to reaching much higher pressure excursions (49‰ for S_1, 137‰ for S_2 and 133‰ for S_3) than those experienced during the linear elastic tests (always < 3‰). In the linear elastic tests, force variations ΔF had never exceeded 40 kN, whilst here ΔF = 135 kN when the first cavity opens and ΔF = 152 kN when all the cavities are open. The reason for the failure is probably the imperfect quality of the sealing between the steel feedthrough and the electric pins, a topic still under development. Using different sealing technologies and/or more compliant shapes of the steel tap ring are possible countermeasures currently under consideration. After opening, the pressure measured by the sensors rapidly increases

and then eventually stabilizes at the value of the environmental pressure (in all three cases larger than the initial reference pressure p_0 corresponding to the sealing of the cavity). After opening, the calculation of volume variations and the prediction of the force in the bar become obviously meaningless. In Figure 14c and 14d the volume variation reconstruction and the force prediction are therefore interrupted, for each measuring unit, at the instant of the corresponding sealing failure. On the other hand, temperature variations after opening basically track ambient excursions (Figure 14b), with the only exception of the immediate aftermaths of the bar rupture (occurring around t = 3800 s), where a sudden temperature increase is observed, particularly in S_3, probably caused by the thermal energy released during rupture.

The second fundamental difference is the evidence of the inadequacy of the reconstructed volume variations (Figure 14c) to track the applied force variations beyond the linear elastic range of the bar mechanical behaviour. Figure 14d clearly shows that, by using the linear correlation expressed by Eq. (6) with the proportionality coefficients k_1, k_2 and k_3 obtained from test #1, the estimated force time-histories increasingly diverge from the applied force time history as the bar enters into the inelastic domain. At the instant of sealing failure, the estimated forces are in fact 10 to 20 times larger than the actual one, and this ratio would have been even much greater if the cavities had not opened. Focusing on the initial stage of the test, the same Figure 14d shows that the assumed linear correlation provides a very good matching until about 50 kN for the whole of the three measuring units, after that becoming progressively less accurate. This proves, on the one hand, that all the tests reported in Section 5.3 really correspond to the bar linear response domain, and, more importantly, on the other hand, that the presence of the holes significantly reduces this linear domain with respect to standard non-drilled bars, as a consequence of the stress concentration around the hole. It is also important to notice that the present monotonic test does not allow to definitely conclude about the elastic or inelastic nature of the observed nonlinearity. This is left for future investigations. In any case, the inadequacy of the linear correlation between volume variation and applied force proposed measuring system to track inelastic forces is well expected and obviously due to the cavity volume variations directing reflecting not the static but the kinematic state of the bar (like, in fact, ordinary strain gages). With this premise, it still might be of interest to understand whether the cavity volume variation can accurately track the bar displacement beyond the linear elastic range. Figure 15a reports the experimentally obtained correlations between the reconstructed cavity volume variations and the applied force, confirming that linearity is confined within the initial range of ΔF = 50 kN (roughly corresponding to $(\Delta V/V_0)_F$ = 2‰). Similarly, Figure 15b reports the experimentally obtained correlations between the reconstructed cavity volume variations and the displacements across the cavities measured by the three strain transducers. Like in Figure 15a, in Figure 15b still linearity appears restricted to the same initial range of ΔL_i = 0.025 mm and $(\Delta V/V_0)_F$ = 2‰, but here the

sensitivity of the volume to the displacement appears much more stable. Especially, the three curves in Figure 15b clearly appear proportional to each other. This suggests that a nonlinear relation between volume variations and bar elongation, similar to that expressed by the curves reported in Figure 15b, might be used to accurately tracking the axial deformations of the instrumented bar, even in the fully nonlinear range of its mechanical response.

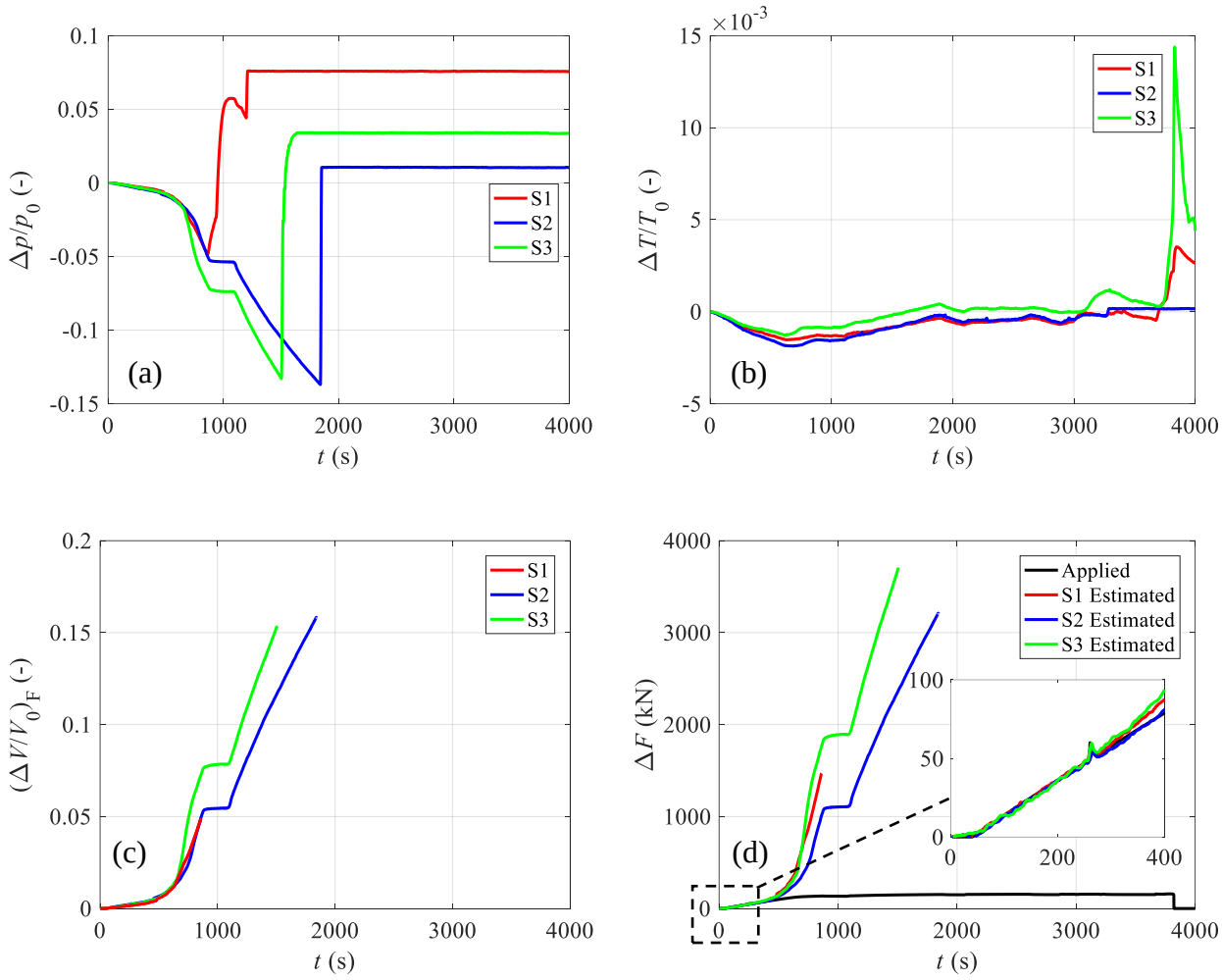

Fig. 14. Monotonic tensile test until rupture: (a) measured pressure; (b) measured temperature; (c) reconstructed force-dependent volume; (d) applied vs estimated force. Note: volume-to-force calibration as from test #1.

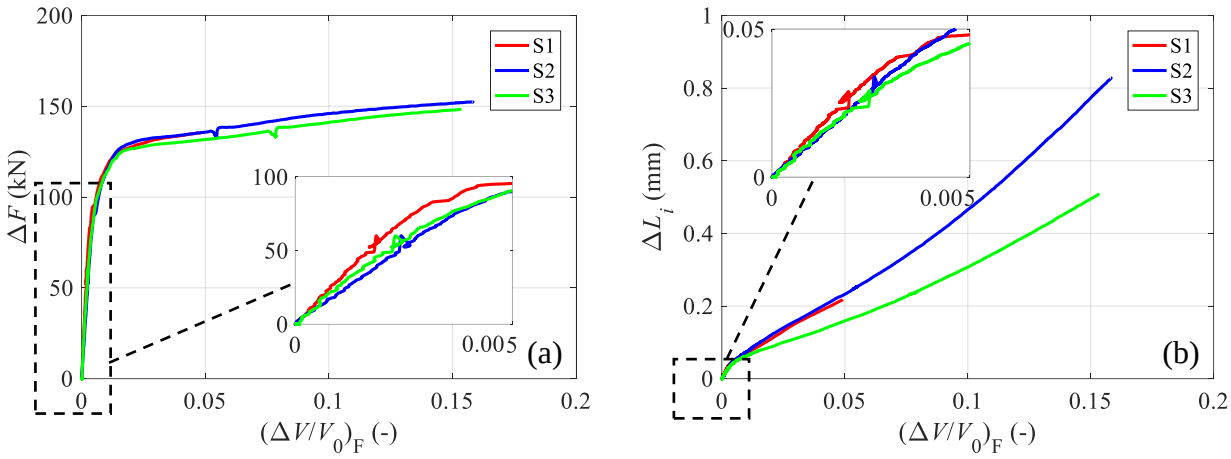

Fig. 15. Monotonic tensile test until rupture: (a) experimental correlations between cavity volume variations and applied force; (b) experimental correlations between cavity volume variations and bar elongations around the holes.

6. Discussion

The reported tests performed on a steel reinforcing bar demonstrate the effectiveness of the S3 system. The operating principle of S3 is based on the continuum mechanic law which states that a uniaxial state of stress induces on a structural element a volume variation. If the volume variation is observed in a cavity full of fluid surrounded by continuum, the monitoring of the fluid state variables gives a measure of the uniaxial stress. The presence of the cavity determines specific stress concentrations localized around the cavity. Stress concentrations are physiological in reinforcing bars, localized in the external ribs ensuring the necessary bond between steel and concrete [15]. Because steel reinforcing bars in RC structures do not usually suffer significant fatigue problems during their service life, significant stress concentration factors are still compatible with their use.

The results presented in the previous paragraphs demonstrate that, in the elastic range, the volume variation of the cavities, evaluated from pressure and temperature collected by MEMS, can be linearly correlated to the external force and, consequently, to the axial strain of the bar. The range of proportionality is limited due to the stress concentration induced by the presence of the cavities that reduce the yielding load. In this range, the static and the cyclic tests, both in tension and in compression, performed on the steel bar equipped with three measuring units show a good accuracy in tracking the applied external load. The average tracking error at zero load is less than an equivalent axial stress of 2 MPa, corresponding to an axial strain of 10 μm/m. These results show that, although the presence of the cavity certainly modifies the local strain field, the initial calibration properly identifies the relation existing between the

measurement and the force or, equivalently in the linear range, between the measurement and the strain field around the hole.

The test exploring the nonlinear behaviour of the bar up to collapse clearly shows the loss of proportionality between the volume variation and the applied load. Nevertheless, the comparison of S3 measurements with the data collected by three extensometers mounted across the cavities shows a nearly proportional correlation of the volume variation with the axial elongation over a broader range of displacements. The nonlinear correlation between volume variations and axial elongations further demonstrates S3 effectiveness as a local strain measurements device. The maximum strain around the hole measured by S3 before failure is about 2.1% in average (if the 25mm base of the strain transducers is adopted), which is comparable with the 2.5% claimed by FOS manufacturers.

The match between the applied load and the estimated one is encouraging especially because of the low-cost of the system that uses only a MEMS sensor. The test also shows that, although the technology of the electrical feedthrough is under study, a good survivability of the sealing up to high deformations has already been achieved. With a guaranteed accuracy of ±0.1 hPa, the currently adopted MEMS sensor implies an overall accuracy of about ±5 MPa in terms of stresses in the bar (i.e. of about ±25 μm/m in terms of strains), as long as the bar responds in the linear range. This is acceptable at the present state of this study but more accurate sensors will be appropriate for real applications.

The feasibility of S3 is also related to the two following issues.

The first regards the installation process. Whether installed in a new construction or in an existing one, the smart bar is expected to arrive at the building site already instrumented and cabled, the sensor being embedded into the bar in the processing centre, right after bar cutting and forming. In the case of a new construction, the instrumented bar will be incorporated in the steel cage as an ordinary bar, only providing that the cable pin will touch the formwork. In the case of an existing construction, the instrumented bar will be welded to existing bars or inserted among them, after removing and before restoring the concrete cover. In any case, investigations are currently under way, in conjunction with a steel producer, to standardize and industrialize the manufacturing of the smart bar, particularly the drilling and sealing processes.

The second issue relates to the code compliance of the instrumented bar. Because of the cavity the bar is not as structurally efficient as an ordinary bar of the same diameter. To date, there are three ways to avoid this problem: (i) the bar is only used as a sensor, with no structural purpose; (ii) the bar is also used as a structural element with reduced strength and ductility, and the overall sectional response is computed accordingly; (iii) the bar is also used as a structural element but, as detailed in S3 patent [14], its diameter is locally enlarged around the hole, in order to replicate

the mechanical behaviour of an ordinary bar. This final way requires further analytical and experimental studies and is not in the scope of this paper.

7. Conclusions

This paper introduces the concept of a technology for monitoring the axial strain in reinforcing steel bars by measuring pressure and temperature variations occurring in a cavity drilled in the bar, using commercially available, low cost MEMS sensors. The use of the perfect gas law together with an initial thermal calibration makes it possible to correlate the cavity volume variation with the axial load applied on the reinforcing bar.

At first, the basic theoretical principles are explained and used to derive useful calibration and operation formulas, expressing the correlations between the main thermo-mechanical variables.

Then, tests are conducted to ascertain the feasibility and accuracy of the new sensing system. In particular, a thermal calibration test is conducted in temperature controlled conditions under zero axial load, providing the temperature corrections formulas. A mechanical calibration test is then conducted through a set of different load steps in environmentally uncontrolled conditions, providing the correlation between each of the three cavity volume variations and the imparted axial force. The force estimation capability of the three S3 system is finally explored by performing a comprehensive set of static and dynamic tests, which show a good accuracy in terms of force estimation and linearity in elastic range. The results are encouraging considering the early development stage of the tested prototype, and further improvements are expected regarding all key components of the system. The type of MEMS sensors used in this research can work over a pressure range that is quite appropriate for monitoring strain variations in RC structures. Furthermore, it is specifically designed for tolerating large mechanical shocks, which makes it suitable to construction sites. Indeed, these sensors are commonly used in a much more aggressive environment than the one in which S3 is placed, where they are sealed into a steel chamber, so a long durability of the proposed system is expected. This technology is intended to be integrated into reinforcing steel bars aiming to a modular monitoring system that has the single bar as a unit and that leverages the versatility and readability of MEMS to equip smart structures.

The system can be embedded also in other types of reinforcing materials able to host a cavity that can be sealed and for every field and every geometrical setup where strain measurement is required.

References

[1] Bremer, K, Weigand, F, Zheng, Y, Alwis, LS, Helbig, R & Roth, B 2017, 'Structural Health Monitoring Using Textile Reinforcement Structures with Integrated Optical Fiber Sensors', *Sensors*, vol. 17, no. 345, pp. 1-12.
[2] Spencer, BF Jr., Park, J-W, Mechitov, KA, Jo, H & Agha, G, 2017, 'Next generation wireless smart sensors toward sustainable civil infrastructure', *Procedia Engineering*, vol. 171, 5-13.
[3] Lynch, JP & Loh, KJ 2006, 'A summary review of wireless sensors and sensor networks for structural health monitoring', Shock Vib. Digest, vol. 38, no. 2, 91-128.
[4] Mutlib, N.K, Baharom, S.B., El-Shafie, A., Nuawi, M.Z., 2016, 'Ultrasonic health monitoring in structural engineering: Buildings and bridges', Structural Control and Health Monitoring, 23(3), 409-422.
[5] Alavi, A. H., Hasni, H., Lajnef, N., Chatti, K., 2016 'Continuous health monitoring of pavement systems using smart sensing technology', Construction and Building Materials, 114, 719-736.
[6] Ge, Y., Elshafie M. E. B., Dirar, S., Middleton, C. R., 'The response of embedded strain sensors in concrete beams subjected to thermal loading', Construction and Building materials, 70, 279-290.
[7] Montanini, R., Recupero, A., De Domenico, F. & Freni, F., 2016, 'Strain sharing assessment in woven fiber reinforced concrete beams using fiber Bragg grating sensors', Sensors (Switzerland) 16 (10), .
[8] Hester, D., Brownjohn, J., Bocian, M. & Xu, Y., 2017, 'Low cost bridge load test: Calculating bridge displacement from acceleration for load assessment calculations', Engineering Structures 143 (7), 358-374.
[9] Prieto, M., Tanner, P., Andrade, C., Fernandex, M. 2013 'Experimental and numerical study of bond response in structural concrete with corroded steel bars', IABSE Workshop on Assessment, Upgrading and Refurbishment of Infrastructures; Rotterdam, Netherlands, 1752-1759.
[10] Quiertant, M, Baby, F, Khadour, A, Marchand, P, Rivillon, P, Billo, J, Lapeyrere, R, Toutlemonde, F, Simon, A & Cordier, J, 2012, 'Deformation monitoring of reinforcement bars with a distributed fiber optic sensor for the SHM of reinforced concrete structures', *NDE 2012*, 1-10.
[11] Barrias, A, Casas, JR & Villalba, S 2016, 'A review of distributed optical fiber sensors for civil engineering applications', *Sensors*, vol. 16, no. 748, 1-35.
[12] Mains, R. M., 1951, 'Measurement of the distribution of tensile and bond stresses along reinforcing bars, ACI Journal, 48 (11), 225-252.
[13] Lagier, L., Massicotte, B., Charron JP 2016,' Experimental investigation of bond stress distribution and bond strength in unconfined UHPFRC lap splices under direct tension', Cement and Concrete Research, 74, 26-38.
[14] Tondolo, F 2016, 'Embedded system for measurements of strain/stress in one-dimensional elements', *Patent* n° 102016000118077, Italy.
[15] Zheng, H., Abel, A, 1998, 'Stress concentration and fatigue of profiled reinforcing steels', International Journal of Fatigue, 20(10), 767-773.